RESEARCH ARTICLE | APRIL 07 2025

Accurate electron densities from quantum Monte Carlo calculations using real-space grids

Alexander Kaiser; Stephan Kümmel

J. Chem. Phys. 162, 134108 (2025)
https://doi.org/10.1063/5.0250838

The Journal of Chemical Physics ARTICLE pubs.aip.org/aip/jcp

Accurate electron densities from quantum Monte Carlo calculations using real-space grids

Cite as: J. Chem. Phys. 162, 134108 (2025); doi: 10.1063/5.0250838
Submitted: 27 November 2024 • Accepted: 12 March 2025 •
Published Online: 7 April 2025

Alexander Kaiser and Stephan Kümmel[a)]

AFFILIATIONS

Theoretical Physics IV, University of Bayreuth, 95447 Bayreuth, Germany

[a)]Author to whom correspondence should be addressed: stephan.kuemmel@uni-bayreuth.de

ABSTRACT

We provide accurate energies and electronic densities for Li_2, C, and N_2 from the diffusion Monte Carlo (DMC) method in the fixed node approximation based on orbitals from a real-space grid approach. With relatively simple single-determinant trial wave functions, we demonstrate the benefits of an all-electron approach in conjunction with a highly accurate grid method for calculating the orbitals that build the determinant. Our DMC ground state energies match with those of more elaborate single-reference quantum Monte Carlo (QMC) methods based on orbital basis sets. The binning technique is revisited to calculate the electronic density on a spatial grid. We examine the dependence of the resulting mixed estimator and extrapolated density on the trial wave function, specifically on the density functional generating the orbitals, by employing two distinctly different functionals, namely, the local density approximation and the exact-exchange functional. Residual statistical artifacts in the QMC densities are readily corrected by using a regularization method, resulting in smooth densities. As an example for the insight that can be gained from an accurate density, we verify that in the carbon atom, the density along one specific direction can have an asymptotic decay that differs from the decay found in all other directions. We relate this observation to previously published work, which discussed the implications that such a nodal feature may have for the exact Kohn–Sham potential.

I. INTRODUCTION

Quantum Monte Carlo (QMC) methods are very attractive for calculating the correlated wavefunction of many-electron systems and corresponding expectation values because of their high *ab initio* accuracy. Electronic structure calculations for real-world materials on the other hand typically rely on density functional theory (DFT) because of its favorable ratio of accuracy to computational cost. The central observable of DFT is the one-body ground state density, which is guaranteed to be the true density of the interacting system when the exact exchange–correlation (xc) functional is used. Having available accurate ground-state densities is of great interest for DFT development for several reasons. First, when the exact density is known, the Kohn–Sham scheme can be inverted to yield the exact xc potential. This has been for years, and to this day continues to be, an important way for gaining valuable insight into the exact functional and the properties of xc approximations.[1–21] Second, while the quality of xc approximations is often assessed from evaluating energies and observables, such as bond lengths and barrier heights, it has been pointed out that xc development should aim more directly at reproducing the density,[22,23] and important insights can be gained from directly comparing densities.[21,24–26] Third, having accurate densities is of interest in itself because properties of a many-particle system, e.g., ionization energies, can be reflected in topographical features of density, with orbital nodal surfaces serving as an important example.[27–33] In line with these observations, the development of methods that allow for accurately calculating the electron density continues to be a field of undiminished research interest.[34]

The wave function-based QMC and in particular fixed-node diffusion Monte Carlo (FNDMC) method, its most widely used flavor,[35] in principle, grants access to highly accurate densities. However, the density of a molecular system is a much more intricate quantity than, for example, its ground state energy or variance, for a number of reasons: it is a spatially resolved, feature-rich function that spans several orders of magnitude with distinct features such as cusps at the nuclei and an exponentially decaying asymptotic tail. Ultimately, the full information of the true ground state is encoded in these features of the density, as we know from the Hohenberg–Kohn theorem. Furthermore, the density operator does

not commute with the Hamiltonian, introducing a systematic bias in its estimation, if not corrected for. Nevertheless, densities are frequently calculated from QMC methods.[36,37] In order to evaluate the QMC densities not only visually but making them suitable for successive analysis, a solid regularization scheme is needed to handle the statistical fluctuations that are an inevitable aspect of QMC methods. Especially when inverting such densities via the inverse Kohn–Sham map, i.e., finding the auxiliary Kohn–Sham potential to reproduce the density, every impurity of the density can become a major hindrance in the inversion process. Furthermore, since most inversion techniques rely on the density in a local (point-wise) way without the ability to incorporate statistical errors in the algorithm, such errors directly enter the target xc potential.

Most QMC methods employ atom-centered basis sets[35,38–40] or plain waves[37] to represent the single-particle orbitals.[41] Although such basis sets often offer a computationally efficient and elegant description, representing the nodal surface in FNDMC reliably can require special care.[42] A successful alternative is offered by different types of grid-based techniques.[43,44] In our work here, we take the step toward completely and exclusively representing the orbitals and the density on a real-space grid. A specific advantage of such a real-space grid approach is its generally systematic and, in a loose sense, even variational convergence. The major problem of real-space grids is the computational expense that would result from treating the three-dimensional space with a uniform, Euclidean grid, while maintaining the spatial resolution to capture the rapid orbital oscillations in the vicinity of the nuclei. In this paper, we report FNDMC calculations that use orbitals from a real-space grid. The specific calculations that we present here exploit that one can design non-equidistant grids that increase the number of points close to the nuclei via a bifocal layout;[45] see Fig. 1. While this special grid design yields a very good ratio of accuracy to computational cost, it limits our present work to atoms and diatomic molecules. The concepts for the grid-based evaluation that we present in the following are, however, completely general, i.e., not specific to the bifocal setup. Future work may combine them with grid-based techniques that allow for solving electronic structure problems in general geometries, e.g., as discussed in Ref. 46. In this first study, we limit the wave function to a relatively simple Slater–Jastrow form with a single determinant and a Jastrow function of Padé form for the sake of transparency. We can, thus, specifically focus on the merits and challenges that come with a grid-based approach. In addition, we also focus on the techniques to evaluate the density.

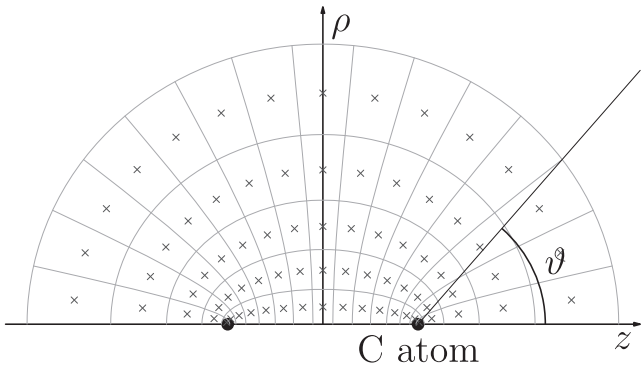

FIG. 1. Sketch of the prolate spheroidal grid transformed to cylindrical representation. The crosses indicate the grid points and are concentrating at the two foci at $z = \pm a$, represented by the black circles. Each grid point is located in its grid cell. Grid cells far from the focal points have larger volume, while grid cells in their vicinity are small. In this example, the focus at $z = -a$ is vacant, while the other is occupied with a carbon atom at $z = +a$. For the analysis of the angle-resolved decay rate in Sec. V C, we setup straight lines starting from the carbon atom with an angle of ϑ with the z axis.

Different approaches can be used for generating the single-particle orbitals that underlie the QMC calculation: Hartree–Fock (HF),[38] general valence-bond or natural orbitals,[42,47] or the direct optimization of orbital- or basis-set parameters.[35] Furthermore, in recent years, great progress has been made in developing techniques that optimize the representation of the wavefunction.[48] In our work here, we chose DFT orbitals from two distinctly different approximations, the local density approximation (LDA) and the exact-exchange functional (EXX). For the latter, we construct a local, multiplicative potential in the Krieger–Li–Iaftrate (KLI) approximation.[49] Using this set of techniques, we calculate ground-state energies and densities for three paradigm systems: the molecules Li_2 and N_2, and the C atom. The energies that we obtain compare well to those of orbital-basis set based single-determinant QMC calculations with considerably more elaborate Jastrow functions. We analyze the influence of the orbitals (LDA vs EXX) on the QMC results and discuss the robustness with which densities are obtained. The correlated electron density that we obtain for the C atom shows a different asymptotic decay in the specific direction that is characterized by a nodal surface of the highest occupied orbital in the corresponding Kohn–Sham system. This shows that such topographical features, the existence and relevance of which has been discussed from different perspectives in the past,[28,30,32,33] can indeed be found in the interacting system.

Our paper is structured as follows: in Sec. II, we briefly review some central elements of FNDMC calculations that are relevant to our work. Section III explains the real-space grid that we use, and Sec. IV details the calculation of the particle density. We then present our results in Sec. V, and we close with a summary and conclusions in Sec. VI. The supplementary material offers technical details about our calculations, the density regularization procedure, and makes available the density data files and additional plots of the densities.

II. SHORT REVIEW OF DIFFUSION MONTE CARLO

Diffusion Monte Carlo (DMC) is an elaborate method to accurately calculate ground state properties. It is based on the imaginary-time propagation rewritten as a diffusion equation[50] with importance-sampling.[51] Detailed outlines of DMC are presented, e.g., in Refs. 52 and 53. In the following, we summarize its main aspects. The Schrödinger equation is recast as

$$-\partial_\tau f(\mathbf{R},\tau) = \left[-D\nabla^2 + \nabla\cdot\mathbf{u}(\mathbf{R}) - S(\mathbf{R})\right] f(\mathbf{R},\tau), \qquad (1)$$

a diffusion equation for the importance-sampled probability density $f = \Psi_T\Psi$, where Ψ_T is usually the best approximation to the true wave function available for evaluation and Ψ is the desired ground state. The drift velocity $\mathbf{u} = \Psi_T^{-1}\nabla\Psi_T/2D$ and the source term $S = E_R - E_L$ are expressions of the trial wave function, where the local energy $E_L = \Psi_T^{-1}\hat{H}\Psi_T$ represents the action of the Hamiltonian $\hat{H}$,

the diffusion constant $D = \hbar^2/2m_e$ in SI units represents the electron mass, and E_R is a reference energy connected to normalization.

The diffusion equation is solved stochastically by employing an approximation to its true Green function, which propagates f by a given time step. To this end, the probability function f is realized by an ensemble of weighted walkers, viz. $(\lambda, \mathbf{R})$, where $\mathbf{R} = (\mathbf{r}_1, \ldots, \mathbf{r}_n) \in \Omega^n$ is a point in configuration space, holding all electrons coordinates $\mathbf{r}_i \in \Omega \subset \mathbb{R}^3$, and λ is an associated weight. The stochastic representation of f reads

$$f(\mathbf{R}, \tau) = \sum_k \lambda_k(\tau)\delta(\mathbf{R} - \mathbf{R}_k(\tau)), \tag{2}$$

with the normalization constraint $\sum_k \lambda_k = 1$. The walkers undergo a classical stochastic trajectory, which is generated by repetitive application of the Green function of Eq. (1) on Eq. (2) with small time steps. Since the exact Green function is unknown in general, approximations are employed. With a vanishing time step, these approximations converge to the true Green function, while simultaneously inhibiting the propagation of the walkers. Thus, the time step error is often remedied by extrapolating the results of multiple finite time step calculations to zero time step. We use the elaborate approximation to the Green function from Ref. 53 that incorporates the true asymptotic limits of the local energy and the drift near nuclei and nodes, samples from exponential and normal distributions conditionally, refines the source terms, and further lowers the serial correlation of the resulting walker trajectory, allowing for larger and thus more efficient time steps while maintaining small time step errors.

The most fundamental concern about DMC is the fermion sign problem. The framework of stochastic realizations for the diffusion process relies on non-negative probabilities. For a fermionic system, negative signs could naturally arise, and any negative sign of f would contradict positive probabilities. The fixed-node approximation (FNA) alleviates this methodical issue by imposing the nodal structure of the trial wave function Ψ_T upon the ground state Ψ to which the method converges,[54] ensuring their product to be positive. This new stationary state is called the fixed-node ground state, a reasonable approximation to the true ground state in many cases. The resulting flavor of QMC is the so called fixed-node DMC. To converge the fixed-node state to the true ground state, the nodes of the trial wave function need to approach the nodes of the exact ground state. A systematic expansion of the trial wave function in the Slater determinant space would allow representing the exact nodal structure, but comes at the cost of a configuration-interaction scaling in computational cost.

It is, therefore, desirable to utilize sophisticated trial wave functions that incorporate correlation effects in order to decrease the number of determinants in an expansion, or improve the quality of a single determinant wave function. A Jastrow factor is a standard ingredient to describe pair or higher-order particle correlations,[55,56] and a variety of choices for the correlation functions exist.[35,38,39] In this work, we restrict our trial wave function to consist of a single determinant Φ and a simple Jastrow factor J,[55,56]

$$\Psi_T = e^J \Phi. \tag{3}$$

Our Jastrow factor is a two-parameter Padé form for the electron–electron coincidence only, i.e.,

$$J = \sum_{i \neq j} u(|\mathbf{r}_i - \mathbf{r}_j|) \qquad \text{with} \qquad u(r) = \frac{\gamma r}{1 + br}. \tag{4}$$

It is inferior to more sophisticated expansions up to electron–electron–nucleus terms and also to more elaborate forms than the Padé form, yet has been used quite successfully in the literature[38,53] because of its transparency and the reasonable results that can be obtained with it. γ is fixed by the singlet and triplet electron–nucleus cusp condition,[57] but the parameter b can be optimized. Although we could choose individual singlet and triplet parameters for b when either two electrons of opposite or same spin meet, we restrict ourselves to one global parameter. As usual in DMC calculations, we optimize the parameterized trial wave function with variational Monte Carlo (VMC) first and use its optimized version as the DMC trial wave function. In the case of our trial wave function, its nodes do not change upon optimization with respect to the nodes of the determinant itself. Therefore, our VMC optimization (of one single Jastrow parameter b) has no effect on the nodal quality, but only accelerates the DMC calculation by lowering the statistical fluctuations. The single parameter is optimized for minimal energy using a least squares fit of a quadratic polynomial. We emphasize that the use of an all-electron approach with highly accurate orbital cusps renders the use of an electron–nucleus Jastrow term less necessary.

To build the Slater determinants, single-particle orbitals are required. The most commonly used orbitals are from the Hartree–Fock method (HF), although a vast variety of choices exist including natural orbitals or DFT. We use self-consistent DFT orbitals from the LDA and the exact EXX functional, for which the optimized effective potential[58] has been calculated in the KLI approximation[59] (xKLI). From the resulting sets of orbitals, we construct the Kohn–Sham Slater determinant Φ.

We deliberately choose a single determinant to focus our analysis on the quality of the orbitals. Furthermore, sums over determinants have been shown to have a less prominent impact compared to improvements to the orbitals of a single determinant in some cases.[42,52] (Generally, of course, energy gains are obtained from a sum over determinants.) Similarly, a more elaborate Jastrow factor would only affect the statistical fluctuations in a DMC calculation, but neither the nodal structure nor the DMC energy. In our actual calculations, we use the DMC algorithm of Ref. 53. However, we adopt a slightly different treatment of persistent walkers, i.e., walkers that reside at the same location in configuration space for an unjustifiable number of iterations; see the supplementary material, Sec. S2 for details.

III. ALL-ELECTRON ORBITALS ON A GRID

An accurate approach to the computation of all-electron DFT orbitals for diatomic molecules or atoms is the use of specialized grids in a prolate spheroidal (PS) coordinate system, as used in Ref. 45 for DFT calculations. The PS coordinate system has the full cylindrical symmetry, compatible with the symmetry of a diatomic or atomic Hamiltonian. Thus, the orbitals are readily separated in one part reflecting the azimuthal dependency and another two-dimensional part depending on the z coordinate and the distance

ρ to the z axis. The azimuthal part can be solved analytically, yielding rotational integer quantum numbers m that enter the subsequent numerical equations, i.e., the orbitals take the form

$$\varphi_m(\mathbf{r}) = \tilde{\varphi}_m(\nu,\mu)e^{im\phi}, \tag{5}$$

and only $\tilde{\varphi}_m(\nu,\mu)$ is treated numerically. The analytical complex exponential of the orbitals in this representation can be rewritten in terms of sine and cosine to arrive at real orbitals.

The two-dimensional (ν, μ) part is numerically represented on the PS grid in the variables μ and ν, rather than $z = a\cosh\mu\cos\nu$ and $\rho = a\sinh\mu\sin\nu$. With a uniform grid in μ-ν-space, the coordinate transformation concentrates grid points at the two foci $(0, 0, \pm a)$, where a is a parameter of the PS coordinate system. A sketch of the PS grid is shown in Fig. 1. The indicated line starting from the carbon atom under angle θ can presently be ignored, as it is irrelevant for the understanding of the grid and will be explained in Sec. V C. For diatomic molecules, the ions are placed at the foci, with $2a$ being the bond length, while for atoms, one focus is occupied by the atom and the other focus is left vacant. The non-uniform grid in the Euclidean space adapts to all the features of the diatomic system. The grid's resolution at the two foci can be made arbitrarily small, while it is coarse-grained in the regions far from the origin. Depending on the dimensions of the uniform grid, the asymptotic decay, the cusps as well as accurate bonds can be rendered with practically hardly any limits on the numerical resolution.

The key step in combining orbitals from a grid method with QMC is interpolation. In the QMC algorithm, one must be able to evaluate the orbitals at any given point in the electrons' domain. Thus, an interpolation scheme for the grid-based discrete orbitals must be employed that yields continuous values for the orbitals, gradients, and Laplacians. We use BSplines to efficiently represent the orbitals from the grid in continuous space. This is a straight-forward process for the value of the density. In the case of a cylindrical or PS coordinate system, there are different symmetry restrictions to the orbitals. In addition, the gradient and Laplacian in PS coordinates (resembling cylindrical coordinates) include terms that diverge on the z axis, as discussed in detail in Ref. 45. If the orbitals obey the exact symmetries, the divergent terms cancel analytically, but in a naïve numerical approach, this might not necessarily be the case. This imposes strong demands on numerical details of the implementation of the derivatives. To address these issues, we do not rely on direct differentiation of the BSplines. We rather identify well-behaved terms in the gradient and Laplacian and build extra BSplines for them. The details are shown in the supplementary material. To evaluate the derivatives, we evaluate the BSpline of each term and recombine them to yield the wanted derivative. In this way, both symmetries are ensured and divergencies are tempered.

Analytically, the divergence of the kinetic energy at the nucleus cancels with the Coulomb potential, resulting in finite values for the local energy. However, when combining the kinetic part from the BSplined gradient and Laplacian with an analytical potential, the cancellation breaks down in close vicinity to the nuclei. This introduces a bias of the local energy at the cores. This bias is only present in a small region around the nuclei and its spatial extent reduces with finer grids for the orbitals. We investigate this dependence on the grid in the supplementary material, Sec. S1.

Note that the PS grid points never lie on the z axis, i.e., the bare Coulomb singularity is never sampled directly; see Fig. 1. Nevertheless, the grid points approach the z axis systematically with increasing grid accuracy. Any plot against the z axis in this paper is along those PS grid points closest to the z axis, but not the z axis directly. With this numerical setup, we perform spin-polarized all-electron calculations using the DARSEC electronic structure code.[45]

IV. ESTIMATING THE CHARGE DENSITY

A. Binning technique

To capture the electron density with spatial resolution, we use the binning technique. This well-known approach generates a histogram of the underlying density by performing a Bernoulli experiment for each bin at each walker realization. For VMC, where the many-body probability function Ψ_T^2 is known analytically, Ref. 60 introduced an improved estimator for the density, based on derivatives of the trial wave function. In DMC, on the contrary, the probability function $f = \Psi_T\Psi$ is only known in terms of its stochastic realizations, and therefore, improved estimators are more challenging to develop.[61] Another density estimation common for Markov chains in general is kernel density estimation, which can be understood as regularization or smoothing of the Dirac-delta. It maps the walker's location in the configuration space (together with other available information about the walker state, such as derivatives) to some function that estimates the single walker's density. Often kernel density estimation produces visually more appealing representations of the density than a simple histogram would. However, a smoothing of the density has no justification in QMC, e.g., on using kernel density estimation near the nucleus, the underlying kernel would hardly reproduce the electron–nucleus–cusp condition. Therefore, we resort to the binning method in conjunction with our grid.

To start with, the (symmetrized) one-body density operator reads

$$\hat{\mathrm{n}}(\mathbf{r},\mathbf{R}) = \sum_i \delta(\mathbf{r}-\mathbf{r}_i) \tag{6}$$

and will be acting on the probability function f from Eq. (2). To represent the continuous (mixed estimator) density,

$$n(\mathbf{r}) = \int_{\Omega^n} f(\mathbf{R})\hat{\mathrm{n}}(\mathbf{r},\mathbf{R})\,\mathrm{d}\mathbf{R}, \tag{7}$$

we introduce a discretization or binning of the domain of a single electron Ω into subdomains or bins $\{\omega_j\}$, such that, $\omega_j \in \Omega$ pairwise disjoint and $\cup_j\omega_j = \Omega$. The density integrated over any such bin ω is

$$\begin{aligned} N(\omega) &= \int_\omega n(\mathbf{r})\,\mathrm{d}\mathbf{r} = \int_{\Omega^n} f(\mathbf{R})\sum_i \int_\omega \delta(\mathbf{r}-\mathbf{r}_i)\,\mathrm{d}\mathbf{r}\,\mathrm{d}\mathbf{R} \\ &= \int_{\Omega^n} f(\mathbf{R})\sum_i \mathbb{1}_\omega(\mathbf{r}_i)\,\mathrm{d}\mathbf{R} = \mathrm{Exp}\left[\sum_i \mathbb{1}_\omega(\mathbf{r}_i)\right], \end{aligned} \tag{8}$$

where Exp denotes the expectation value and $\mathbb{1}_\omega(\mathbf{r})$ is unity when $\mathbf{r} \in \omega$, and zero otherwise. For sufficiently small bins, where the density has small variations over the bin's extent, the density at some point $\mathbf{r} \in \omega_j$ is approximated by the mean density $n(\mathbf{r})$

$= |\omega_j|^{-1} N(\omega_j)$. Thus, the binning estimator for the density of bin j is

$$\check{n}_j(\mathbf{R}) = |\omega_j|^{-1} \sum_i \mathbb{1}_{\omega_j}(\mathbf{r}_i). \tag{9}$$

Evaluating the expectation of the density value w.r.t. the probability density f yields the estimator of the density at bin j,

$$\begin{aligned} n_j &= \int f(\mathbf{R}) \check{n}_j(\mathbf{R}) \, \mathrm{d}\mathbf{R} \\ &= |\omega_j|^{-1} \sum_k \lambda_k \int \delta(\mathbf{R} - \mathbf{R}_k) \sum_i \mathbb{1}_{\omega_j}(\mathbf{r}_i) \, \mathrm{d}\mathbf{R} \\ &= |\omega_j|^{-1} \sum_{ki} \lambda_k \mathbb{1}_{\omega_j}(\mathbf{r}_{ki}). \end{aligned} \tag{10}$$

To accumulate the density on the entire domain, this results in the following scheme: for every electron i of every walker k, we map the electron's coordinate $\mathbf{r}_{ki}$ to its corresponding bin ω_j and increase the bin's density by the walker's weight over the bin's volume, $|\omega_j|^{-1}\lambda_k$, and repeat this for every time step. We choose our bins ω_j to align with the PS grid cells, sketched in Fig. 1. This has several advantages, as discussed in Sec. IV B.

B. Density fluctuations

The density from any QMC approach comes with a statistical error. With the binning method, the density not only depends on the realization of the walkers' random walk and its inherent fluctuations but also on the volume of the bins. From Eq. (10), electrons visiting small bins cause a greater change in the density than electrons in larger bins, which reflects in the variance of the density. The variance of $\check{n}_j(\mathbf{R})$ w.r.t. a realization of f reads

$$\begin{aligned} \mathrm{Var}\,[\check{n}_j] &= \int f(\mathbf{R}) \check{n}_j^2(\mathbf{R}) \, \mathrm{d}\mathbf{R} - n_j^2 \\ &= |\omega_j|^{-2} \sum_k \lambda_k \sum_{i,i'} \mathbb{1}_{\omega_j}(\mathbf{r}_{ki}) \mathbb{1}_{\omega_j}(\mathbf{r}_{ki'}) - n_j^2. \end{aligned} \tag{11}$$

By splitting the double sum into diagonal and off-diagonal parts, we arrive at

$$\mathrm{Var}\,[\check{n}_j] = n_j\left(|\omega_j|^{-1} - n_j\right) + \rho_j, \tag{12}$$

where

$$\rho_j = |\omega_j|^{-2} \sum_k \lambda_k \sum_{i \neq i'} \mathbb{1}_{\omega_j}(\mathbf{r}_{ki}) \mathbb{1}_{\omega_j}(\mathbf{r}_{ki'}). \tag{13}$$

The first term of Eq. (12) resembles the typical Bernoulli variance of $p(1-p)$, modified to account for the bin size. The additional term ρ_j represents the variance caused by statistical and electronic correlations; its only contributions arise from two electrons of the same walker being in the same bin and thus links the variance of the one-body density to the two-body density. The $|\omega_j|^{-2}$ scaling of the variance is apparent from Eqs. (10) and (12). Thus, smaller bins result in higher fluctuations.

Near a focal point in the PS grid, the bin size becomes small enough to induce larger fluctuations on a small scale; however, the vicinity of the nuclei is a region of high density and great statistical significance. To the contrary, with few walkers visiting the regions far from the nuclei, the increased bin volume counteracts the lack of statistical significance. Using the PS grid cells as bins, the number of walkers visiting an individual bin does not need to span the same range of orders as the density, greatly lowering the fluctuations compared to bins of constant volume. This property of the variance of $\check{n}_j$ reflects in the statistical error of its expectation value n_j.

In the supplementary material, Sec. S3, we propose a conceptually simple *a posteriori* refinement procedure based on extrapolation of the density to remedy the fluctuations in the notorious domains of the QMC density. We will refer to those regularized or refined DMC (VMC) densities as rDMC (rVMC) densities. If not explicitly mentioned, we always report regularized densities.

C. Extrapolation estimator

In DMC, any observable that does not commute with the Hamiltonian suffers from a biased estimation due to the mixed estimator. The density, therefore, only approaches the true or the fixed-node ground state density if the trial wave function approaches the exact ground state. Thus, the DMC density is fundamentally biased by the mixed estimation of its operator. To reduce the bias, extrapolation schemes can be used.[62] Consider the trial wave function Ψ_T and the exact ground state Ψ related by $\Psi = \Psi_T + \delta\Psi$. The exact density and the respective estimators in VMC and DMC are

$$n_0 = \langle \Psi | \hat{n} | \Psi \rangle, \quad n_\mathrm{D} = \langle \Psi | \hat{n} | \Psi_T \rangle, \quad n_\mathrm{V} = \langle \Psi_T | \hat{n} | \Psi_T \rangle. \tag{14}$$

One can project out the first-order errors from the mixed estimator n_D by employing linear or ratio extrapolations, respectively,

$$n_0 = 2n_\mathrm{D} - n_\mathrm{V} + \langle \delta\Psi | \hat{n} | \delta\Psi \rangle, \tag{15}$$

$$= \frac{n_\mathrm{D}^2}{n_\mathrm{V}} - \frac{(n_\mathrm{D} - n_\mathrm{V})^2}{n_\mathrm{V}} + \langle \delta\Psi | \hat{n} | \delta\Psi \rangle. \tag{16}$$

While the ratio scheme of Eq. (16) seems more suitable for a positive quantity such as the density, especially in regions of low density, we do not find major differences between both estimators for the systems under consideration. The dominant error is hence given by $\langle \delta\Psi | \hat{n} | \delta\Psi \rangle$, inaccessible to any further corrections. From Eq. (16), it is tempting to rely on $n_\mathrm{V}^{-1}(n_\mathrm{D} - n_\mathrm{V})^2$ as an indicator for the second-order error of the extrapolation, but it is not clear what fraction of magnitude this term contributes to the total second-order error in comparison with the unknown $\langle \delta\Psi | \hat{n} | \delta\Psi \rangle$. The linear scheme of Eq. (15) is norm-conserving in addition, and therefore, we exclusively use the estimate

$$n_\mathrm{e} = 2n_\mathrm{D} - n_\mathrm{V} \tag{17}$$

to correct for the mixed estimator bias. The magnitude of the mixed estimator bias reflects the magnitude of difference between VMC and DMC wave functions. Generally, the mixed estimator bias can be lowered by a more sophisticated trial wave function, i.e., three-body Jastrow factors, multi-reference determinants, or backflow. An accurate and highly parameterized trial wave function can resemble much of the correlation effects and thus be close to the DMC state. With a trial wave function of high quality, the mixed estimator bias is expected to be small and a linear extrapolation can restore the ground state estimator to a decent accuracy. The

VMC wave function of this work, however, is deliberately kept simple and cannot restore much of the correlation. To validate the extrapolation scheme, we analyze our extrapolated densities and their consistency in Sec. V B.

We will label the extrapolated non-regularized DMC densities as eDMC and the extrapolated and regularized DMC densities as erDMC, where we first apply the refinement procedure to VMC and DMC densities and extrapolate from rVMC and rDMC.

D. Sources of systematic errors of the density

The quality of the density is mainly affected by four sources of error. The statistical error due to the Monte Carlo sampling can be estimated by performing independent calculations of the same density and subsequent standard statistical analysis. Using the PS grid cells as bins for the density, we adapt the binning as much as possible to the two driving factors of the densities variance (density magnitude and bin size). Next, the accuracy of the DMC method within the fixed node approximation depends crucially on the nodal structure of the trial wave function; therefore, our results are subject to the fixed node error. With a single referential determinant, the nodal structure is fully determined by the orbitals and, in conjunction with DFT, by the density functional in use. With the LDA and the exact exchange, we compare two nodal structures. The ultimate benchmark for the quality of the nodes is the comparison of the DMC energy to other methods or the non-relativistic limit. The time step error is systematically examined with extrapolation to zero time step for all of our systems. We choose a time step small enough to render the time step error negligible. Finally, the extrapolation of the mixed estimator is potentially the largest error contribution to our densities. Even with VMC, DMC, and extrapolated densities at hand, the quality of the extrapolated density can only be judged in comparison with other densities. The DMC density directly reflects trends that improve the trial wave function toward a considerably better ground state candidate and can be used without extrapolation to support qualitative results.

V. RESULTS

We have examined the energies and densities for the molecules Li_2, N_2, and the carbon atom. The equilibrium bond lengths are those of Huber and Herzberg[63] rounded to the fourth digit resulting in distances of $R = 5.051$ for Li_2 and $R = 2.0743$ for N_2. The atoms of the molecules are placed at $z = \pm R/2$ in the PS grid, while the carbon atom is located at $z = 1$ on the z axis. Following our grid analysis in the supplementary material, Sec. S1, we choose our grid to have 181×181 grid cells. Throughout this paper, we use Hartree atomic units, unless specified otherwise.

A. QMC energies

To quantify the influence of the time step error, we performed DMC calculations with the time steps 1, 2, 3, 5, 7.5, 10, 15 and 20×10^{-3} a.u. and extrapolated to zero with a quadratic polynomial. Table I lists the resulting energies. The coefficient of determination of the fit was 0.96, 0.99, and 0.99 for Li_2, N_2, and C, respectively. For Li_2, the time step error of the energy at a time step of 0.001 a.u. is less than 10^{-5} a.u., while 1.1×10^{-3} a.u. for N_2 and 4×10^{-4} a.u. for C. Our default time step for the density calculations of 0.001 a.u. is, therefore, within chemical accuracy (1 kcal/mol ≈ 0.0016 a.u.) of the extrapolated energy, indicating a negligible time step error of the densities. In cases in which the time step error becomes important, the recently developed improved scheme of Ref. 64 can be employed.

TABLE I. Energies and percentage of recovered correlation energy E_c from different methods. The referenced calculations in this table use basis set orbitals and employ elaborate Jastrow factors up to three-body terms. Our calculations are spin-polarized with orbitals on a PS grid of dimension 181×181, a simple Padé –Jastrow and a single determinant (SD). We use a time step of 0.001 a.u. and extrapolated to zero for the DMC run based on LDA orbitals. The bottom two rows show the results for multi-determinantial wave functions (MD). References for the HF energy and the non-relativistic limit were taken from Refs. 38, 39, 67, and 68, respectively. The percentage values for the correlation energies given here may differ slightly from the ones given in the cited literature due to small differences in the reference values for the HF energies or the non-relativistic limits. For the sake of transparency and easier understanding of the table, all results of this work are marked by an asterisk.

		$C(^3\Pi_0)$		$Li_2\ (^1\Sigma_g^+)$		$N_2\ (^1\Sigma_g^+)$	
		E	$E_c(\%)$	E	$E_c(\%)$	E	$E_c(\%)$
DFT@LDA	*	−37.468 540	−144.39	−14.724 422	−118.82	−108.695 827	−54.33
DFT@xKLI	*	−37.691 862	0.59	−14.870 580	−0.79	−108.985 178	−1.57
VMC[J + SD]@LDA	*	−37.722 50(2)	20.47(2)	−14.913 02(1)	33.48(1)	−109.089 05(8)	17.36(1)
VMC[J + SD]@xKLI	*	−37.735 69(2)	29.04(1)	−14.930 64(3)	47.70(3)	−109.103 16(5)	19.94(1)
DMC[J + SD][a]		−37.829 66(4)	90.04(3)	−14.991 67(2)	96.99(2)	−109.5039(1)	93.00(2)
DMC[J + SD]		−37.8295(2)[b]	89.9(1)	−14.9911(1)[c]	96.53(8)	−109.487(1)[c]	89.9(2)
DMC[J + SD]@LDA	*	−37.830 37(1)	90.503(8)	−14.991 70(1)	97.02(1)	−109.516 75(3)	95.343(5)
DMC[J + SD]@xKLI	*	−37.830 44(1)	90.548(7)	−14.991 43(4)	96.79(3)	−109.516 86(3)	95.361(5)
DMC[J + SD]@LDA, ext.	*	−37.830 71(4)	90.72(3)	−14.991 83(9)	97.11(7)	−109.5183(3)	95.62(5)
DMC[J + MD][a]		−37.836 20(1)	94.287(5)	−14.994 56(1)	99.322(8)	−109.5206(1)	96.04(2)
DMC[J + MD]		−37.840 80(6)[b]	97.27(4)	−14.9938(1)[c]	98.71(8)	−109.505(1)[c]	93.2(2)

[a]Toulouse and Umrigar, 2008, Ref. 35.
[b]Buendía *et al.*, 2009, Ref. 39.
[c]Filippi and Umrigar, 1996, Ref. 38.

Optimization of the Padé–Jastrow factor from Eq. (4) determines b to be 1.56, 3.60, and 3.20 for Li_2, N_2, and C, respectively.

Table I shows reference energies and the results from this work. It confirms the well-known fact that the total energies from LDA are not impressive, and the xKLI energies are close to the HF values. VMC, as expected with our simple trial wave function, improves the DFT results only to about 20%–50% correlation energy, while Refs. 35 and 38 recover up to 80% with a single determinant and high-quality Jastrow factors (not shown in the table). The DMC energies from the real-space grid are in very good agreement with the references based on basis sets, increasing the recovered correlation in all cases but Li_2@xKLI (where @xKLI, here and in the following, denotes the origin of the orbitals). The improvement ranges from about 0.5% to 0.8% for carbon, 0.1% to 0.6% for Li_2, and 2.3% to 5.7% for N_2.

While LDA- and xKLI-based trial wave functions recover significantly different amounts of correlation in VMC, the DMC energies are remarkably independent of the DFT functional, indicating a strong alignment of their nodal structure. We also found the Kohn–Sham orbitals of the LDA and xKLI to have remarkable spatial similarity (not shown). Although slight deviations in the orbitals could lead to larger differences in their determinant's nodes and thus the DMC energy, this does not seem to be the case in the systems that we studied.

The review on single-determinant DMC results for Li_2 of Bressanini *et al.*,[42] where basis sets up to $6s4p2d1f$ were investigated, exemplifies the challenges associated with finding a basis set that reliably represents the nodal structure. Inclusion of some orbital character even increases the DMC energy by decreasing the node quality, while careful optimization of the basis set results in a very accurate DMC energy of −14.9923(2).[42] Considerable effort must be invested to explore the large space of the basis sets even in the case of a molecule as small as Li_2.

In the real-space grid approach, convergence of the orbitals and thus the nodal surface is very transparent and systematic, and a situation where including "unsuitable" basis functions lowers the nodal quality does not occur. We find a monotonous convergence of the DMC energy as a function of our grid spacing, i.e., there is only one parameter that is optimized. In practice, we do this in seven steps, cf. the supplementary material Sec. S1. It is further interesting to note that while on the one hand, the one-determinant VMC energy of −109.4520(5) reported in Ref. 35 for N_2 is noticeably lower than our VMC energy of −109.103 16(5) due to the better Jastrow factor that was used in Ref. 35, on the other hand, our one-determinant DMC energy using the real-space grid, −109.5183(3), is lower than the literature value for the one-determinant DMC energy[35] of −109.5039(1).

The optimal nodes representable with a single determinant are generally unknown, except for small systems of high symmetry.[42] Taking the wave function of Ref. 42 as a proxy for this limit, the nodal manifold from our real-space grid orbitals is within a third of chemical accuracy to this proxy. To avoid misunderstandings, we would like to again stress that our single-determinant calculations with a simple Jastrow factor cannot compete with more highly refined DMC calculations in terms of the obtained total energies,[65,66] but the purpose of our work is to demonstrate the advantages of using a real-space grid.

B. Densities

The DMC density for Li_2 based on a calculation that started from LDA orbitals is shown in Fig. 2. The representation of the density uses the same grid as used for the orbitals. We plot the density on a logarithmic scale to highlight its high resolution and global smoothness. The density accurately shows its distinct features: the nuclear cusps of purely exponential form are present at the Li nuclei. The asymptotic decay is continuous up to radii of about 12–15 a.u. and density values of order 10^{-7}. Beyond this domain, the noise slowly starts to increase in the low-density regime—an inevitable feature of MC at low probabilities. Despite the density values ranging from 10^{-10} at boundaries of the simulation box to 10^{1} at the nuclei, the density is smooth throughout the physically relevant domain. Plotting the density with a linear instead of a logarithmic scale or with iso-surfaces could not render any of the mentioned fluctuations. Here, the beneficial effect of the spatially varying size of the PS grid cells comes into play, effectively sampling larger bins in regions of low density and small bins at the nuclei. The σ-type bond is visible between the atoms upon closer inspection; see Fig. 3 for a more detailed view of this region.

Let us shortly estimate the computational demands to recover a smooth density from QMC. With a total of N_r walker realizations in a QMC calculation, any bin ω is stochastistcally visited by an average of $N_r n|\omega|$ walkers, where n is the average density over the extent of the bin. For instance, bins at which the density of Fig. 2 has decayed to 10^{-8} have volumes of about 0.1 to $1a_0^3$. For those bins to be visited 100 times during the QMC run, one requires a total number of walker realizations of about 10^{10}–10^{11}. In our calculations of the density, we aim for $N_r > 10^{11}$. To make efficient use of our computational infrastructure, 6.4×10^5 walkers are propagated in parallel. The number of propagation steps in our calculations is around 6×10^5. In practice, we reach reasonable computation times by parallelizing the calculations over several hundred cores. Although the serial correlation is greatly reduced by the parallel sampling, we used data blocking with a block length of 25 to reduce the

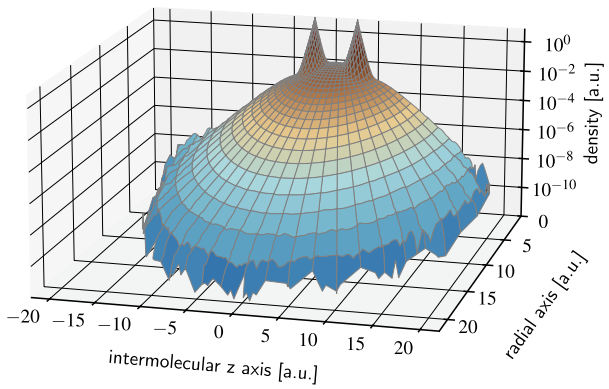

FIG. 2. Bare DMC density of Li_2 based on LDA orbitals. The density is smooth up to density values of the order 10^{-7}, rendering the density without significant noise to a radial extent of about 15 a.u. From there on, stronger fluctuations build up until the density values are dominated by noise at distances of about 20 a.u. The color reflects the magnitude of the density. Note that the curved (gray) lines indicate straight lines in the PS coordinate system, but do not correspond to the PS grid, which is more fine-grained.

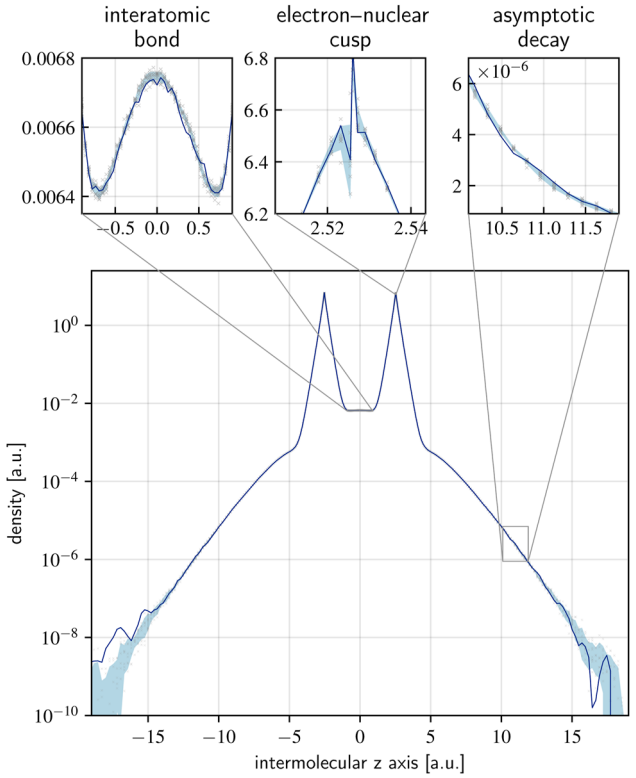

FIG. 3. Estimated error of the DMC@LDA density for Li_2. From independent density calculations, we estimated the standard deviation of a single density realization. The dark blue line shows a realization of the density, while the light blue halo region is its standard deviation. Note that the confidence band is the error of a single realization, not of the mean of all calculations. For clarity of visualization, we plotted the confidence band around the mean of all density calculations. The gray crosses indicate the sampled densities. While the global plot scales the density logarithmically, the insets do not.

remaining serial correlation in the sample averaged over the parallel walkers.

To estimate the statistical error of the DMC density, we performed ten independent calculations of the density. Standard statistics yield the error halo for the DMC density, shown in Fig. 3 along the molecular axis. The statistical error of the density in the physically relevant domains is not recognizable by eye. We again chose to show the logarithmic density to visualize the asymptotic realm, where the fluctuations of the density are bound to increase. We heavily zoomed in on the most intricate features of the density: the cusp, the inter-atomic partition, and an asymptotic region, where the density is at the edge of actual physical relevance.

As expected, the error increases in the region far from any nucleus, since only a small fraction of electrons ever visits this region. However, even in the logarithmic representation, the error at low density turns out to be quite small, with a relative value of about 6% at a density of 2×10^{-6}. In the entire moderate to high-density region, the relative error becomes negligible, effectively vanishing within the linewidth.

Between the nuclei, the density takes values of about 6.6×10^{-3} and shows a variation stemming from the σ bond on the order of 4×10^{-4} (difference from maximum to minimum), making it a challenging region to describe accurately. The density's absolute (statistical) error constitutes about 2×10^{-5}. Therefore, the relative error of the density is in the range of 3×10^{-3}. The density's σ-bond variation is resolved with an error of about 5%.

While increased stochastic fluctuations of the density close to the grid foci are inevitable due to smaller bins, the wiggles in the "cusp" inset are not of statistical origin only. As discussed in the supplementary material, Sec. S1, some inaccuracies arise from converting the discrete grid-representation of the orbitals' derivatives to continuous space.

The refinement procedure, presented in the supplementary material, Sec. S3, can be used to remedy any of the remaining artifacts discussed above. For example, a systematic error occurs in the immediate vicinity of the nuclei due to the larger variance that results from small bins, and the evaluation of the numerical derivatives, cf. supplementary material, Sec. S3. However, this error is embedded in the much larger domain of exponential decay due to the cusp condition; therefore, the proper cusp can readily be restored with the extrapolation scheme that we discuss in detail in the supplementary material. This analysis shows that the acquired density is overall suitable not only for visual inspection but also for subsequent analysis with high numerical requirements, e.g., inversion of the density to its Kohn–Sham potential.

The orbitals that build the trial wave function can have a major influence on the DMC density. With a single-determinant, the orbitals alone define the nodal structure and, therefore, the quality of the DMC ground state. The electronic structure of the carbon atom with four electrons in the up-channel and two in the down-channel in combination with the orbital nodal line of the highest occupied (molecular) orbital (HOMO), further discussed in Sec. V C, make this system challenging to handle. The DFT densities of LDA and xKLI differ significantly from each other, and thus, the carbon atom is a well-suited, natural test case for investigating how DMC results depend on the starting orbitals. The DFT and DMC densities (spin-up) are presented in Fig. 4 for the carbon atom. The DMC energies obtained from LDA and xKLI are very similar, compare Table I; therefore, one would expect that their DMC densities should also be similar. We find this to be true in the high-density regime. However, the DMC density shows a non-negligible dependence on the functional at lower density, most prominently seen in the insets for the asymptotic decay shown in Fig. 4 at $z \approx 5$ a.u. For xKLI, the DMC and DFT densities almost match, which underlines the quality of the DFT density from xKLI. Since the xKLI approximation incorporates the correct $-1/r$ asymptotic decay of the exact xc potential, it is not surprising that it performs better than LDA, for which the potential decays exponentially. The DMC@LDA density does not fully converge to the DMC@xKLI density in the asymptotic region, but one sees that the features stemming from the LDA are partially corrected for.

The densities show a different peak value at the nucleus, leading to the conclusion that the different methods locally predict different densities. This is a side-effect of the density normalization since any non-norm-conserving change in the density leads to a global multiplicative shift in the density and, therefore, different values at its cusp.

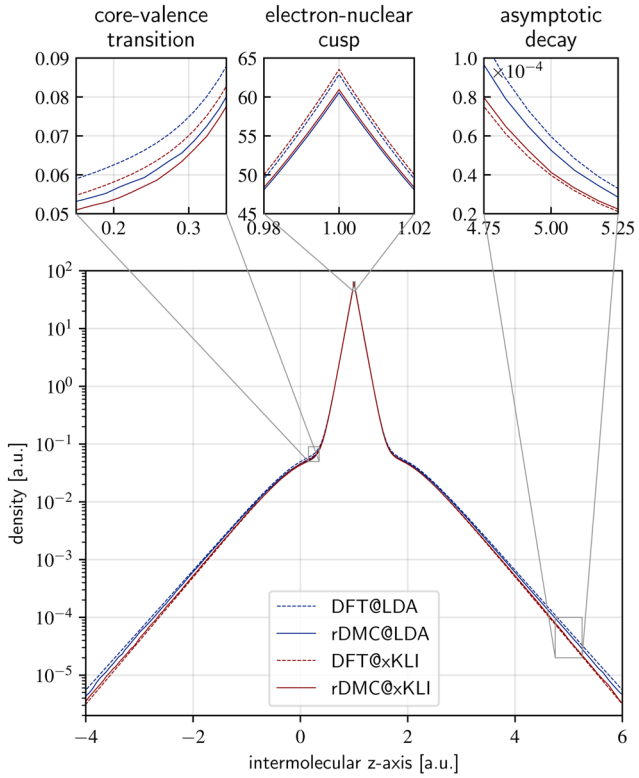

FIG. 4. Investigation of the orbital-dependence of DMC densities. We compare the DFT and refined DMC (mixed estimator) spin-up densities for LDA and xKLI orbitals for the carbon atom. The solid lines show the DMC densities and the dashed lines their DFT counterpart. The values from LDA and xKLI are represented in blue and red, respectively.

One might be surprised by the noticeable orbital-dependence of the DMC density, given that the DMC energies hardly showed such a dependence. However, the finding becomes understandable at least partially as a consequence of the different character of the observables. While both are evaluated with the mixed estimators, only the density suffers from the mixed estimator bias. Therefore, the DMC densities in Fig. 4 have a stronger dependence on the trial wave function, as the DMC process samples $\Psi_T\Psi$, not Ψ^2. Another reason for why the density shows a more pronounced dependence on the starting orbitals than the energy is the "probability regime" in which these observables are evaluated. While the energy is only marginally affected by regions of low wave function probability, the density is essentially capturing these regions with spatial resolution. Thus, the energy depends only weakly on the quality of the nodal manifold in low probability regions, if at all. The density, however, can discriminate nodal quality differences in those low-probability regions. Therefore, one can find different densities that yield very similar energies.

We have found qualitatively similar results for Li_2 and N_2, but on the quantitative level, the orbital dependence is much weaker for these molecules than for the carbon atom. This can at least partially be explained by the observation that the LDA and xKLI orbitals are very similar for Li_2 and N_2 and thus essentially represent the same starting point for DMC.

To assess the impact of the mixed estimator bias and its correction from Eq. (17), we next investigate the quality of the mixed estimator extrapolation scheme from Sec. IV C. Therefore, we inspect the DFT, VMC, DMC, and extrapolated density of the carbon atom based on LDA orbitals shown in Fig. 5. While the detailed behavior of the densities is not important to estimate the extrapolation quality, the differences of the densities are, and especially the comparison of DMC and VMC results. While small in the core-valence region, the density difference is noticeable at the cusp and in the asymptotics. If the deviation of the density due to $\Psi - \Psi_T$ is beyond linear scaling, the extrapolation could not restore the unbiased density. From the densities generated with the LDA alone, one could not draw a conclusion, since a second-order deviation cannot be remedied and we have no indication of leaving the linear regime. Luckily, by comparison with the extrapolated densities generated from xKLI, we can assert such behavior. The orbitals of xKLI differ significantly from the orbitals of the LDA, as discussed in Sec. V C. These differences are reflected in the QMC densities. If the extrapolation was incorrect, LDA and xKLI would yield different extrapolated densities. In Fig. 5, we plot all the densities, including the extrapolated

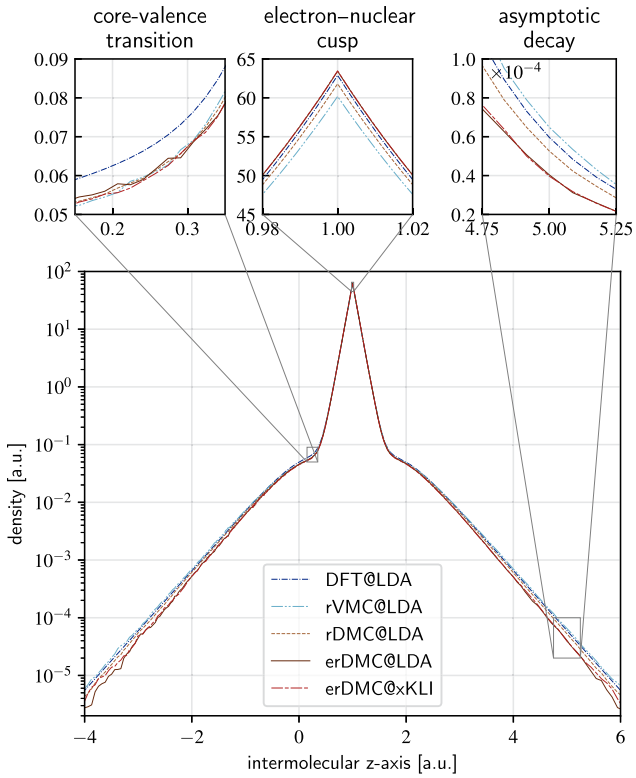

FIG. 5. Demonstration of the quality of the mixed estimator extrapolation: plots of the DFT, rVMC, rDMC, and erDMC densities for the carbon atom based on LDA and the erDMC density from xKLI orbitals. Although DFT, VMC, and DMC lead to somewhat different densities in certain regions of space, the extrapolations based on xKLI and LDA align perfectly. This is not due to LDA and xKLI being the same starting point; see Fig. 4. All the densities are spin-up densities.

ones. The extrapolated xKLI density is in perfect agreement with the one based on LDA; this not only indicates that the deviations remain within the linear regime but also verifies the extrapolation. The bias of the mixed estimator, therefore, can efficiently be eliminated. We note in passing that for Li_2 and N_2 also the extrapolated densities from LDA and xKLI are in good agreement.

C. Orbital nodal features in the carbon atom density

The energy minimizing density that one obtains for the carbon atom with the LDA or EXX functionals is not spherically symmetric. The $^3\Pi_0$ ground state is reflected in a single-particle occupation scheme that follows Hund's rule, $1s^2 2s^2 2p^2_{\uparrow\uparrow}$. While the spin-down channel has no explicit p-orbital character, in the spin-up channel, the two (degenerate) HOMO orbitals are of p-type with $l = |m| = 1$. Schematically, one can think about their angular dependence in the form

$$\varphi_{\mathrm{H}}(r, \vartheta, \phi) \sim r \sin\vartheta e^{-Zr/2} e^{\pm i\phi}, \tag{18}$$

although one should keep in mind that the orbitals realized in an actual DFT calculation are not of the exact hydrogen-orbital form of Eq. (18). However, this form illustrates the aspect that is decisive for the following discussion: this carbon-atom density realizes the special situation of a nodal surface in the orbital density of the highest occupied orbital(s),[69] with a nodal line along the z axis, where $\vartheta = 0$. Situations with a nodal surface of the highest occupied orbital have found special interest in DFT,[28,30,32,33] e.g., because of their possible consequences for the asymptotic structure of the xc potential.

The nodal surface induces a non-spherically symmetric decay of the carbon atom density of the following schematic form:

$$n = n_{\mathrm{R}} + n_{\mathrm{H}} = n_{\mathrm{R}} + 2|\varphi_{\mathrm{H}}|^2, \tag{19}$$

where n_{R} is the residual density without contributions from the HOMO orbital. While the HOMO orbital dominates the exponential decay anywhere except $\vartheta = 0$, the HOMO-1 orbital governs the decay along $\vartheta = 0$, or $z = 0$ equivalently. Since DFT guarantees an exact density for the exact xc potential, the density has solid physical meaning—beyond any doubts about the auxiliary character of Kohn–Sham quantities such as eigenvalues and orbitals.

In the following, we analyze densities that result from DMC calculations, i.e., from beyond the single particle representation, with respect to the question of whether they show the characteristic features that are associated with the nodal surface. To this end, we calculate two densities, DMC@LDA and DMC@xKLI, and analyze their asymptotic decay.

We implicitly define the spatially resolved asymptotic exponential decay rate γ for a density n by

$$n(\mathbf{r}) = n_0(\hat{\mathbf{r}}) \exp^{-\gamma(\hat{\mathbf{r}})r} \tag{20}$$

at $|\mathbf{r}| \to \infty$, where $\hat{\mathbf{r}} = \mathbf{r}/|\mathbf{r}|$. As any bound density decays exponentially,[70] γ can at most depend on the angles, $\gamma(\hat{\mathbf{r}}) = \gamma(\vartheta, \phi)$, for large $|\mathbf{r}|$. Due to symmetry restrictions from the PS coordinates and the doubly occupied p-type orbital from Eq. (18), γ in our case can only depend on ϑ.

We now aim to quantify the value of $\gamma(\vartheta)$ for different angles ϑ. For every ϑ, we consider a straight line starting from the carbon atom and forming an angle ϑ with the z axis; see Fig. 1 for a sketch. For example, $\vartheta = 0$ represents a line from $(0, z_{\mathrm{C}})$ to $(0, z_{\max})$ in cylindrical coordinates, while $\vartheta = 90^\circ$ yields the line from $(0, z_{\mathrm{C}})$ to $(\rho_{\max}, z_{\mathrm{C}})$. Along this straight line, we construct the density by interpolating from its values on the PS grid. Such radially extending slices of the density are shown in Fig. 6. Although the densities at $\vartheta = 90^\circ$ and 180° show a distinct gap in their magnitude, it is their slope that holds the information about the decay rates. For every slice, we fit the density along the line to the exponential form of Eq. (20), omitting the core region ($r < 2.5$ a.u.) as well as the asymptotic region dominated by noise ($r > 4$ a.u.). This yields the decay rate as a function of the angle $\gamma(\vartheta)$. The coefficient of determination in all fits exceeded 0.999, confirming that we consistently fitted only the pure asymptotic decay with our choice for the radial interval. Furthermore, we do not use the density from our refinement procedure to calculate the decay rate.

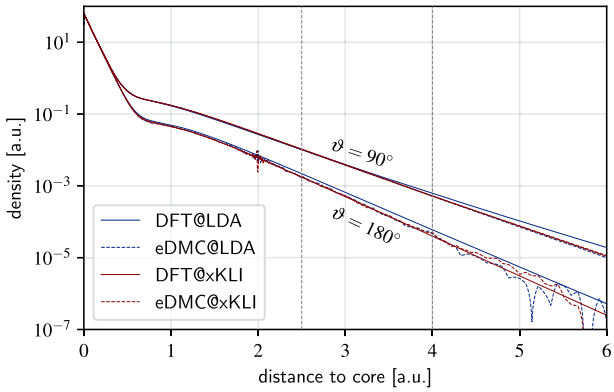

FIG. 6. DFT and eDMC density along the z axis ($\vartheta = 180^\circ$) and the angle $\vartheta = 90^\circ$ are shown for the functionals LDA and xKLI. We fit the graphs in the indicated interval from 2.5 to 4 a.u.. Visually, it is difficult to distinguish the decay rates γ (slope) from the amplitudes n_0 (offset); see Fig. 7 for the angle-dependence of γ. We plot the decay along $\vartheta = 180^\circ$ instead of $\vartheta = 0^\circ$, since the PS grid is more fine-grained on the negative part of the z axis than on the positive side, see Fig. 1.

The results are shown in Fig. 7 for eDMC and DFT densities based on LDA and xKLI. The decay rates from eDMC align with the rate from DFT@xKLI. They approach their extrema at 0° and 90° with quadratic behavior, which reflects the node of second order of the orbital-densities, since the HOMO orbitals have a node of first order and the HOMO density results from squared orbitals. The LDA underestimates the decay for all angles. This is a consequence of the decay rate being coupled to the HOMO eigenvalue[70] by $\gamma = 2\sqrt{-2\varepsilon_{\mathrm{H}}}$ and the well-known fact that ε_{H} of LDA does not accurately reflect the true density decay. However, the decisive observation is that also the DMC densities show a substantial change in the decay rate when ϑ varies from 90° to 0° (or 90°–180°). Thus, the DMC densities show the signature of the nodal line in a very similar way as the DFT densities. The results further show that this is not caused by the potential shortcoming of the DMC method to not be able to change the density in the asymptotic region: One can clearly see that the DMC calculation changes the density in the asymptotic region, as the decay rate of the DFT@LDA density is changed significantly by the subsequent DMC calculation.

The finding that the density obtained from the DMC method shows the characteristic features of the nodal line is of relevance in

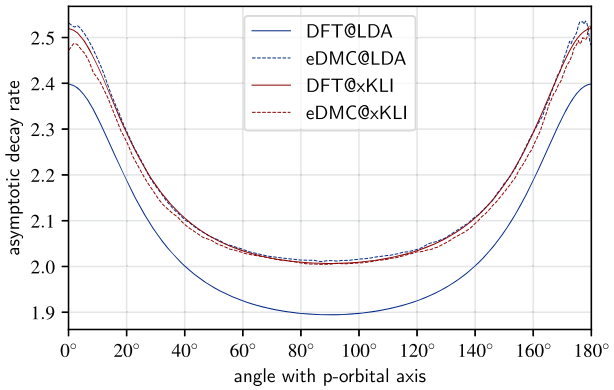

FIG. 7. Asymptotic decay of the densities is dominated by the lower rate of the HOMO 2*p* orbital over a large range of angles, but approaches the larger rate of the HOMO-1 decay of 2*s*-type when approaching the *z* axis or the angles 0° and 180°, equivalently. This behavior is observed irrespective of the functional or method. The values of γ near an angle of $\vartheta = 0°$ and 180° show some noise. This is due to the interpolation on the grid, which becomes a slightly inferior extrapolation when approaching the *z* axis, since the grid points do not lie on the *z* axis directly.

the context of the question whether the (exact) Kohn–Sham potential can have a uniform asymptotic decay, or must be expected to have unusual, potentially diverging features in some regions of space: These different options have been discussed in detail based on an expansion in Dyson orbitals in Ref. 32. Following the work of Gori-Giorgi *et al.*, the observation that the ground-state density shows a different decay along the nodal surface leads to the conclusion that the corresponding (exact) Kohn–Sham potential can be expected to decay regularly, without unpleasant surprises on or in the vicinity of the nodal plane.

VI. SUMMARY AND CONCLUSION

In this paper, we report DMC calculations for atoms and diatomic molecules based on orbitals that are represented on a real-space grid. The grid representation allows for a systematic and accurate convergence of the orbitals. With relatively simple single-determinant trial wave functions, our calculations thus capture large parts of the correlation energy. We furthermore discuss how the electron density can reliably be calculated from a DMC calculation based on the binning technique in combination with the mixed estimator extrapolation. The fluctuations inherent to QMC calculations can efficiently be suppressed by appropriate choices for the bins and by exploiting exact properties of the wave function.

We investigate the dependence of the DMC results on the starting orbitals by comparing QMC calculations that start from LDA orbitals to ones that start from exact-exchange KLI orbitals. Densities show a greater dependence on the starting point than energies, yet can also be calculated reliably over many orders of magnitude and large regions of space. Using these techniques, we show that nodal features that arise in the density of the carbon atom in a DFT calculation as a consequence of building the density from single-particle orbitals are also observed in the DMC density.

While in our work here, we use prolate spheroidal grids that are tailored toward all-electron calculations in real-space, the techniques that we developed are general and can also be used in combination with other numerical setups, e.g., Cartesian grids with underlying pseudopotentials. We hope that the accurate densities that can thus be generated can serve as an input to different types of calculations in the future, e.g., Kohn–Sham inversions that will allow obtaining further insight into exact properties of DFT.

SUPPLEMENTARY MATERIAL

In the supplementary material, we publish our calculated densities: for each system (Li_2, N_2, C), the densities for each method (DFT, VMC, DMC), for each generating density functional of the orbitals (LDA, xKLI), and for each spin-channel are available. In addition, densities for different grids and from several independent calculations are provided for Li_2. The grid-dependence of the energies and the densities are examined in a convergence analysis for the grid parameters in Sec. S1 of the supplementary material. Our approach to deal with persistent walkers is explained in Sec. S2 of the supplementary material. Furthermore, we present in detail our refinement procedure to obtain smooth densities in Sec. S3 of the supplementary material.

ACKNOWLEDGMENTS

We thank T. Lebeda for stimulating discussions.

AUTHOR DECLARATIONS

Conflict of Interest

The authors have no conflicts to disclose.

Author Contributions

A.K. and S.K. together conceptualized the work. A.K. did all the programming, ran all calculations, and generated all tables and figures. Both authors discussed the results and wrote the manuscript together.

Alexander Kaiser: Conceptualization (equal); Data curation (lead); Investigation (equal); Software (lead); Visualization (lead); Writing – original draft (equal); Writing – review & editing (equal). **Stephan Kümmel**: Conceptualization (equal); Funding acquisition (lead); Investigation (equal); Project administration (lead); Supervision (lead); Writing – original draft (equal); Writing – review & editing (equal).

DATA AVAILABILITY

The data that support the findings of this study are available within the article and its supplementary material.

REFERENCES

[1] Y. Wang and R. G. Parr, Phys. Rev. A **47**, R1591 (1993).
[2] C. J. Umrigar and X. Gonze, Phys. Rev. A **50**, 3827 (1994).

[3]Q. Zhao, R. C. Morrison, and R. G. Parr, Phys. Rev. A **50**, 2138 (1994).
[4]O. V. Gritsenko, R. van Leeuwen, and E. J. Baerends, Phys. Rev. A **52**, 1870 (1995).
[5]C. Filippi, X. Gonze, and C. J. Umrigar, in *Recent Developments and Applications in Density-Functional Theory*, edited by J. M. Seminario (Elsevier Science, Amsterdam, 1996).
[6]C. Filippi, C. J. Umrigar, and X. Gonze, J. Chem. Phys. **107**, 9994 (1997).
[7]A. Savin, C. J. Umrigar, and X. Gonze, Chem. Phys. Lett. **288**, 391 (1998).
[8]M. J. Allen and D. J. Tozer, Mol. Phys. **100**, 433 (2002).
[9]D. P. Chong, O. V. Gritsenko, and E. J. Baerends, J. Chem. Phys. **116**, 1760 (2002).
[10]M. Lein and S. Kümmel, Phys. Rev. Lett. **94**, 143003 (2005).
[11]A. M. Teale, F. De Proft, and D. J. Tozer, J. Chem. Phys. **129**, 044110 (2008).
[12]M. Thiele, E. K. U. Gross, and S. Kümmel, Phys. Rev. Lett. **100**, 153004 (2008).
[13]A. S. de Wijn, M. Lein, and S. Kümmel, Europhys. Lett. **84**, 43001 (2008).
[14]M. Thiele and S. Kümmel, Phys. Rev. Lett. **112**, 083001 (2014).
[15]O. V. Gritsenko, Ł. M. Mentel, and E. J. Baerends, J. Chem. Phys. **144**, 204114 (2016).
[16]Y. Suzuki, L. Lacombe, K. Watanabe, and N. T. Maitra, Phys. Rev. Lett. **119**, 263401 (2017).
[17]A. Kaiser and S. Kümmel, Phys. Rev. A **98**, 052505 (2018).
[18]E. Fabiano, S. Śmiga, S. Giarrusso, K. J. Daas, F. Della Sala, I. Grabowski, and P. Gori-Giorgi, J. Chem. Theory Comput. **15**, 1006 (2019).
[19]R. Garrick, A. Natan, T. Gould, and L. Kronik, Phys. Rev. X **10**, 021040 (2020).
[20]A. Aouina, M. Gatti, S. Chen, S. Zhang, and L. Reining, Phys. Rev. B **107**, 195123 (2023).
[21]V. B. Kumar, S. Śmiga, and I. Grabowski, J. Phys. Chem. Lett. **15**, 10219 (2024).
[22]M. G. Medvedev, I. S. Bushmarinov, J. Sun, J. P. Perdew, and K. A. Lyssenko, Science **355**, 49 (2017).
[23]A. Wasserman, J. Nafziger, K. Jiang, M.-C. Kim, E. Sim, and K. Burke, Annu. Rev. Phys. Chem. **68**, 555 (2017).
[24]O. V. Gritsenko, P. R. T. Schipper, and E. J. Baerends, J. Chem. Phys. **107**, 5007 (1997).
[25]D. Cremer, Mol. Phys. **99**, 1899 (2001).
[26]V. Polo, E. Kraka, and D. Cremer, Mol. Phys. **100**, 1771 (2002).
[27]F. Della Sala and A. Görling, J. Chem. Phys. **116**, 5374 (2002).
[28]F. Della Sala and A. Görling, Phys. Rev. Lett. **89**, 033003 (2002).
[29]S. Kümmel and J. P. Perdew, Phys. Rev. B **68**, 035103 (2003).
[30]T. Aschebrock, R. Armiento, and S. Kümmel, Phys. Rev. B **95**, 245118 (2017).
[31]T. Aschebrock, R. Armiento, and S. Kümmel, Phys. Rev. B **96**, 075140 (2017).
[32]P. Gori-Giorgi, T. Gál, and E. J. Baerends, Mol. Phys. **114**, 1086 (2016).
[33]P. Gori-Giorgi and E. J. Baerends, Eur. Phys. J. B **91**, 160 (2018).
[34]L. Cheng, P. B. Szabó, Z. Schätzle, D. P. Kooi, J. Köhler, K. J. H. Giesbertz, F. Noé, J. Hermann, P. Gori-Giorgi, and A. Foster, J. Chem. Phys. **162**, 034120 (2025).
[35]J. Toulouse and C. J. Umrigar, J. Chem. Phys. **128**, 174101 (2008).
[36]R. Q. Hood, M. Y. Chou, A. J. Williamson, G. Rajagopal, R. J. Needs, and W. M. C. Foulkes, Phys. Rev. Lett. **78**, 3350 (1997).
[37]S. Chen, M. Motta, F. Ma, and S. Zhang, Phys. Rev. B **103**, 075138 (2021).
[38]C. Filippi and C. J. Umrigar, J. Chem. Phys. **105**, 213 (1996).
[39]E. Buendía, F. J. Gálvez, P. Maldonado, and A. Sarsa, J. Chem. Phys. **131**, 044115 (2009).
[40]K. M. Rasch, S. Hu, and L. Mitas, J. Chem. Phys. **140**, 041102 (2014).
[41]C. A. Melton and L. Mitas, Phys. Rev. B **102**, 045103 (2020).
[42]D. Bressanini, G. Morosi, and S. Tarasco, J. Chem. Phys. **123**, 204109 (2005).
[43]M. Casula, C. Filippi, and S. Sorella, Phys. Rev. Lett. **95**, 100201 (2005).
[44]A. Aspuru-Guzik, R. Salomón-Ferrer, B. Austin, and W. A. Lester, Jr., J. Comput. Chem. **26**, 708 (2005).
[45]A. Makmal, S. Kümmel, and L. Kronik, J. Chem. Theory Comput. **5**, 1731 (2009).
[46]O. Cohen, A. Brandt, and L. Kronik, J. Chem. Theory Comput. **9**, 4744 (2013).
[47]D. Bressanini and G. Morosi, J. Chem. Phys. **129**, 054103 (2008).
[48]R. Assaraf, S. Moroni, and C. Filippi, J. Chem. Theory Comput. **13**, 5273 (2017).
[49]J. B. Krieger, Y. Li, and G. J. Iafrate, Phys. Rev. A **46**, 5453 (1992).
[50]J. B. Anderson, J. Chem. Phys. **65**, 4121 (1976).
[51]J. W. Moskowitz, K. E. Schmidt, M. A. Lee, and M. H. Kalos, J. Chem. Phys. **77**, 349 (1982).
[52]B. M. Austin, D. Y. Zubarev, and W. A. Lester, Jr., Chem. Rev. **112**, 263 (2012).
[53]C. J. Umrigar, M. P. Nightingale, and K. J. Runge, J. Chem. Phys. **99**, 2865 (1993).
[54]P. J. Reynolds, D. M. Ceperley, B. J. Alder, and W. A. Lester, Jr., J. Chem. Phys. **77**, 5593 (1982).
[55]R. Jastrow, Phys. Rev. **98**, 1479 (1955).
[56]R. B. Dingle, London, Edinburgh Dublin Philos. Mag. J. Sci. **40**, 573 (1949).
[57]T. Kato, Commun. Pure Appl. Math. **10**, 151 (1957).
[58]S. Kümmel and L. Kronik, Rev. Mod. Phys. **80**, 3 (2008).
[59]J. B. Krieger, Y. Li, and G. J. Iafrate, Phys. Rev. A **45**, 101 (1992).
[60]R. Assaraf, M. Caffarel, and A. Scemama, Phys. Rev. E **75**, 035701 (2007).
[61]R. Assaraf and M. Caffarel, J. Chem. Phys. **119**, 10536–10552 (2003).
[62]W. M. C. Foulkes, L. Mitas, R. J. Needs, and G. Rajagopal, Rev. Mod. Phys. **73**, 33 (2001).
[63]K. P. Huber and G. Herzberg, in *Molecular Spectra and Molecular Structure: IV. Constants of Diatomic Molecules*, edited by K. P. Huber and G. Herzberg (Springer US, Boston, MA, 1979), pp. 8–689.
[64]T. A. Anderson, M. C. Per, and C. Umrigar, Chem. Phys. **160**, 104110 (2024).
[65]P. Seth, P. L. Ríos, and R. J. Needs, J. Chem. Phys. **134**, 084105 (2011).
[66]D. Pfau, J. S. Spencer, A. G. D. G. Matthews, and W. M. C. Foulkes, Phys. Rev. Res. **2**, 033429 (2020).
[67]M. V. Ivanov and P. Schmelcher, Phys. Rev. A **60**, 3558 (1999).
[68]D. Sundholm, P. Pyykkö, and L. Laaksonen, Mol. Phys. **56**, 1411 (1985).
[69]T. Schmidt, E. Kraisler, L. Kronik, and S. Kümmel, Phys. Chem. Chem. Phys. **16**, 14357 (2014).
[70]M. Levy, J. P. Perdew, and V. Sahni, Phys. Rev. A **30**, 2745 (1984).